

J-band Synthetic Spectral Fitting

July 27, 2015

In this chapter I describe in detail the process by which I implement an analysis routine to fit RSG synthetic spectra to observed data. The spectra cover the *J*-band, specifically the $1.16 - 1.22\mu\text{m}$ region, where there are various prominent spectral features. These spectral features, arising from elemental absorption, are compared in the observed and model spectra, where the χ^2 -statistic is calculated to assess the goodness of fit for each model. The stellar parameters which are fit for in this analysis are global metallicity $[Z]$, effective temperature (T_{eff}), microturbulence (ξ) and surface gravity ($\log g$). The observed spectra are fit with model spectra from a set of MARCS model atmospheres Gustafsson et al. (2008). Spectra are extracted using the SUI code Bergemann et al. (2012, 2013, 2014) with non-LTE corrections computed for iron, silicon and titanium.

The wavelength range, over which to perform this analysis, is chosen based on the spectral appearance of the region. Typically, in the spectra of cool stars, dense molecular absorption features dominate the spectrum which require high-resolution spectroscopy to distinguish individual features and derive stellar parameters Cunha et al. (2007); Davies et al. (2009a,b). However, in this small wavelength range, the absorption is dominated by well separated elemental absorption features from iron, magnesium, silicon and titanium. Therefore, the spectral resolution required in order to derive stellar parameters is significantly reduced. This means that this analysis can be performed with a relatively small amount of telescope time using multi-object spectrographs like the *K*-band multi-object spectrograph (KMOS) or the multi-object spectrometer for infra-red exploration (MOSFIRE) and is therefore feasible for studies of red supergiant stars (RSGs) in external galaxies.

In addition to this, given the cool temperature of the outer layers of RSGs, the peak brightness of a typical RSG is $\sim 1.1\mu\text{m}$. Combining this with the fact that dust attenuation is significantly lower in the near-IR, compared to the optical regime, RSGs are ideal candidates to be studied at large distances.

Previous implementations of this analysis include that of Davies et al. (2010) and Gazak (2014). This implementation includes aspects of both of these previous implementations and could be described as a hybrid of the two. I approach the implementation in a Bayesian manner which relies on good prior assumptions.

Eventually this analysis routine will be made publicly available which should encourage the community to engage with these routines.

In the remainder of this chapter I first describe the model grids and how they are used in 0.1. I then describe the continuum fitting procedure in 0.2, and go on to detail the method for estimating the bestfit parameters in 0.3. The testing process which these procedures have underwent is described in 0.4, which also includes a comparison between the results produced using this implementation and those of the two previous implementations of the same analysis. Finally, I conclude the chapter in 0.5.

0.1 Model Grid

- How are the grids generated?
- What are the non-LTE corrections?
- What do the current grids look like?
- How could they be improved?

0.2 Continuum Fitting

Accurately matching the continuum levels in the models with that of the observed spectrum provides a base with which to anchor the diagnostic lines. An incorrectly placed continuum level would bias the analysis and result in the strength of the diagnostic lines being over or under estimated producing inaccurate stellar parameters.

There are many factors that affect the level of the continuum and continuum placement, including the resolution of the observations as well as the stellar parameters themselves. Therefore it is vital that when attempting to derive stellar parameters, in crowded regions such as this, the continuum placement is performed consistently and accurately. Intrinsically, when studying RSGs at medium resolution - owing to their cool atmospheres - there are many instances of blended spectral features. At this resolution the density of spectral features creates a pseudo-continuum which in practice is never at the true continuum level. Figure 1 illustrates the varying continuum levels for models where the resolution is varied and Figure 2 shows this affect when varying only the metallicity.

Given that it is impossible to know the true continuum level from any given observation, the scaling applied must be consistent between the models and observations. Scaling is required not only to match the levels of the continuum placement, but also to match the line strengths between the models and observations. Providing the treatment of the models and observations are consistent, the fact that the true continuum is never attained is not significant

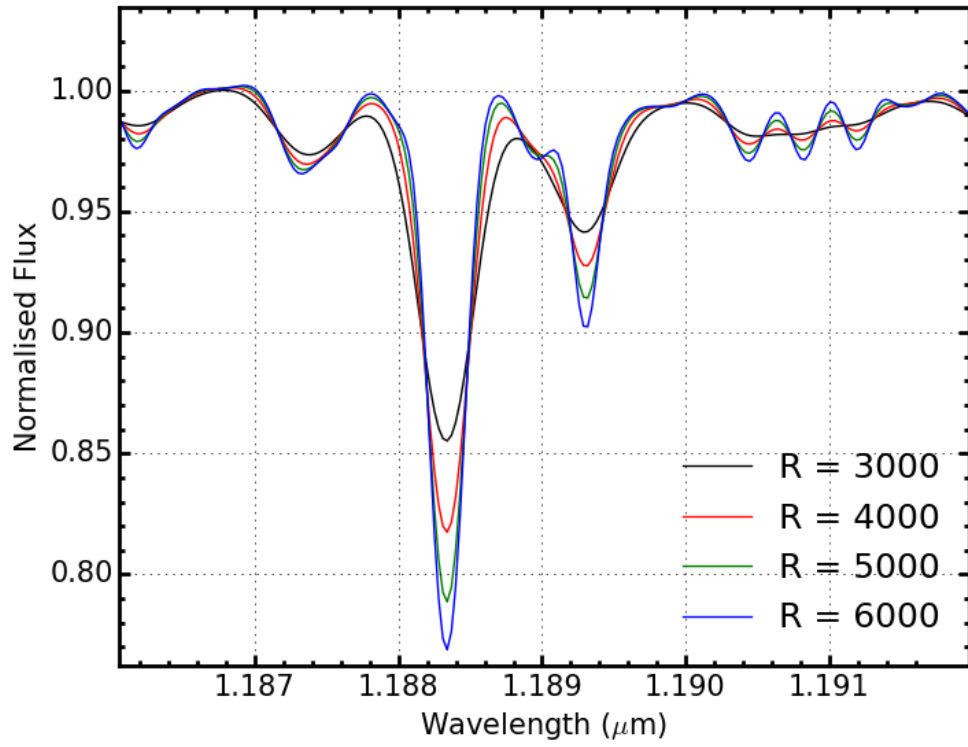


Figure 1 *One model degraded to four different resolution values. This figure demonstrates the how the continuum level changes depending upon the resolution of the spectrum. We see at around 1.191μm at $R = 3000$ the continuum level is perturbed by blended lines.*

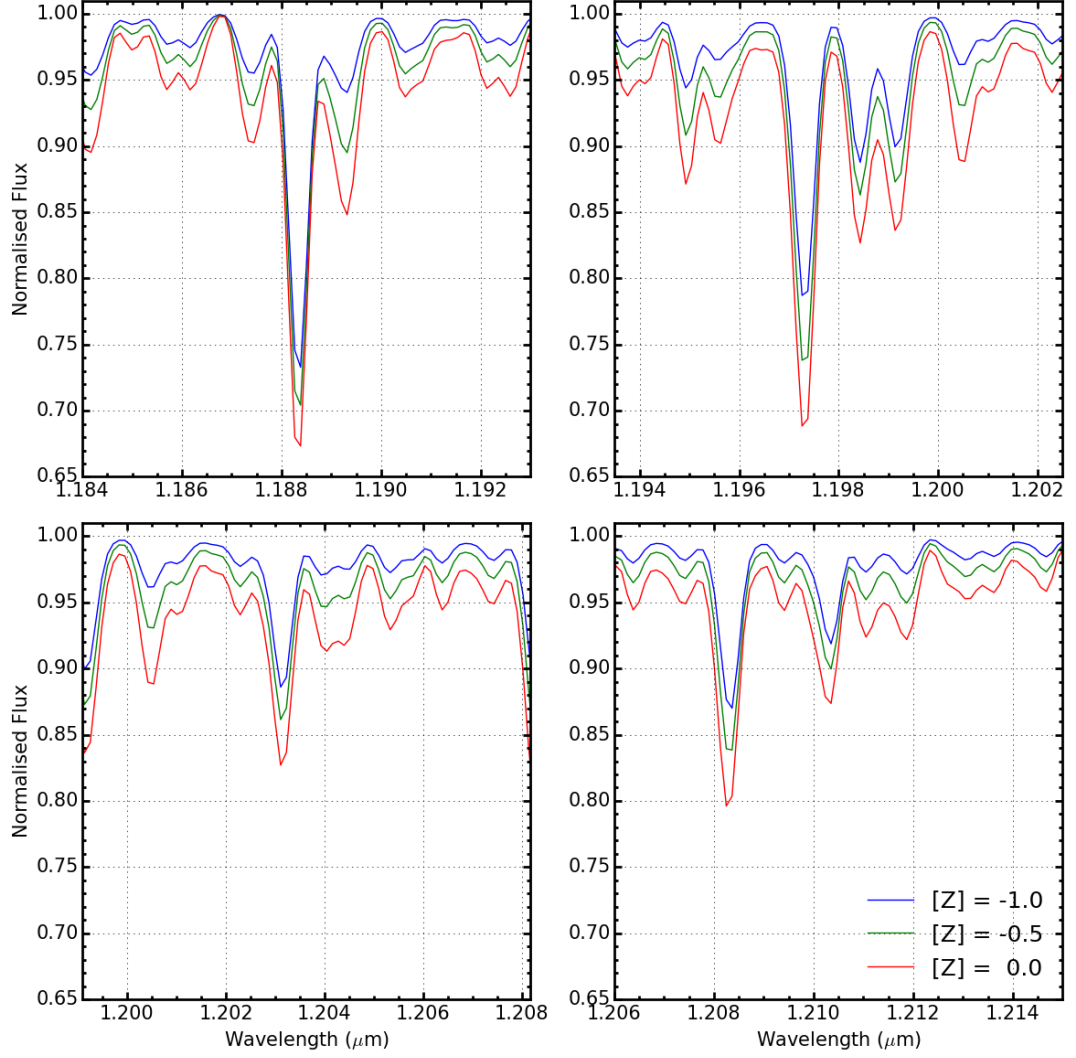


Figure 2 *Three models where only the metallicity is varied. Each panel shows one or more diagnostic line. Metallicity of the model intrinsically affects the continuum level of the spectrum, such that at higher metallicities, there is greater departure from the true continuum level, which in the case of the models is 1.00.*

(Gazak et al., 2014). For this procedure to work effectively, the observed and model spectra should be at the same resolution, have a consistent wavelength calibration and spectral sampling.

In order to account for difference between the spectral sampling in the observed and model spectra, each model spectrum is resampled onto the wavelength scale of the observations by means of a linear interpolation routine. The model spectrum is then degraded to the resolution of the observations by convolving this spectrum with a gaussian filter where the width of the gaussian is defined by the observed resolution. The resolution of the KMOS observations is estimated using the KMOS/esorex pipeline from arc lamp exposures at the appropriate rotator angle for the observations. This is measured for each spectrograph and is assumed to be constant (to within ± 100) across individual IFU's as well as across the detector.

To ensure the spectra are on the same wavelength scale, the observed spectrum is cross-correlated with the model spectrum; a shift is then applied to the observed spectrum in order to minimise the cross-correlation matrix. Over this small wavelength range, one would not expect significant variations in the spectral resolution of the observations to perturb the cross-correlation.

To fit the continuum of the observations first I define the continuum width (cw) as:

$$cw = \frac{\lambda}{R}, \quad (1)$$

where R is the resolution of the spectrum and λ is the wavelength at which the width is taken (in principle this wavelength varies across the spectrum, however, given our spectral window is sufficiently small, I assume $\lambda = 1.20\mu\text{m}$). The continuum width is essentially the resolution element of the spectrum at a wavelength of $\lambda = 1.20\mu\text{m}$.

The model spectrum is divided into wavelength slices each of width $cw\mu\text{m}$ and the maximum of each slice is taken. Figure 3 illustrates that using this technique systematically removes absorption features from the spectrum. In this figure blue points represent the boundaries between the slices of width $cw\mu\text{m}$ and the maximum of each slice is shown in red. Any remaining features in this maximum spectrum are removed by rejecting outliers which are more than 3σ from the mean of the distribution. In figure 3 the $cw \text{ max.}$ points have been through this procedure. This can be seen by noting that the cores of the absorption lines no $cw \text{ max.}$ points present.

The remaining data points (P_{cont}) are used to derive an initial correction function (cf_1) defined using the equation:

$$cf_1 = f\left(\frac{F_{mod}(P_{cont})}{F_{obs}(P_{cont})}\right) \quad (2)$$

where F_{mod} and F_{obs} are the flux in the model and observed spectrum respectively.

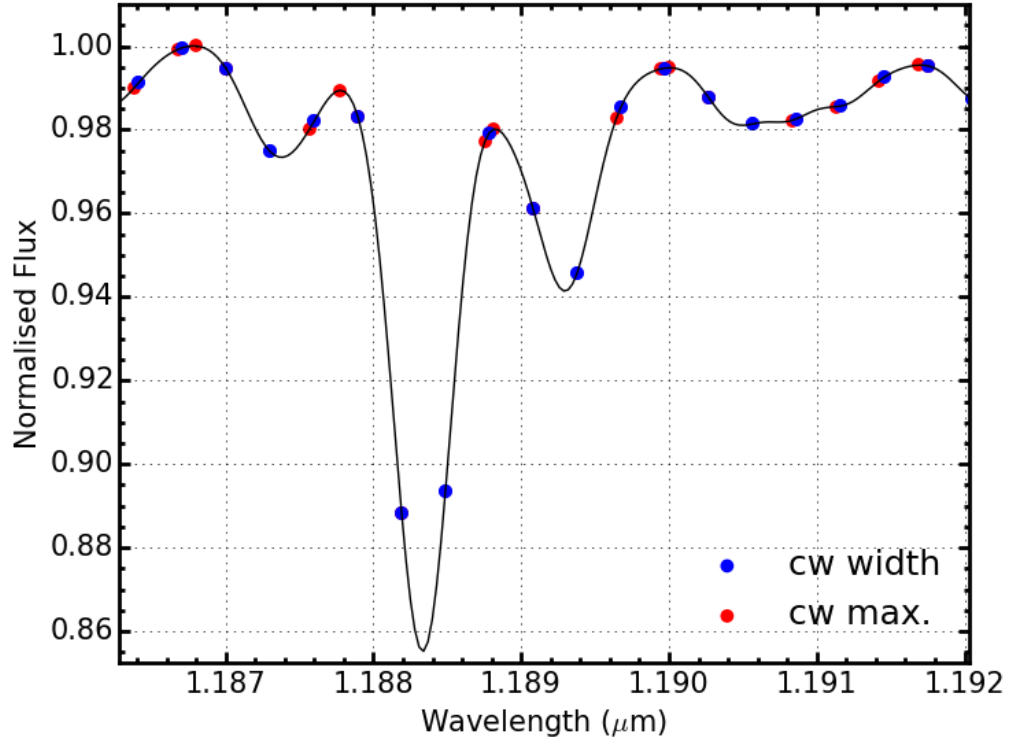


Figure 3 *Illustration of the continuum width (cw) and slicing the model spectrum into regions of $cw\mu m$ is able to remove structure in order to fit the continuum. The solid black line shows an example of a model spectrum degraded to a resolution of 3000, blue points show the boundaries between the slices and red points show the maximum of each slice.*

The final correction function (cf_2), a refinement of cf_1 , is defined by removing outliers more than 3σ from the mean of the correction function cf_1 . This function is used to define the amount of scaling required for the model.

Alternative methods of continuum fitting are discussed in Davies et al. (2010) and Evans et al. (2011). These methods select pseduo-continuum pixels in the models based on ranking the model pixels and selecting a percentage of the pixels with the largest flux. Providing the pixels from the model are selected in this manor and not those in the observations, this is a reliable method with which to derive the continuum level as demonstrated by Davies et al. (2015 in prep.). **What advantage (if any) does the method applied here have over the one used in Davies et al. (2015 in prep.)?**

0.3 Best Fit Parameters

Bestfit paramaters are calcaulted using a chi-squared minimisation approach. Each model in a $21 \times 19 \times 11 \times 9$ model grid is compared to the observed spectrum and a chi-squared value is calculated using the equation,

$$\chi^2 = \frac{1}{N_{pix}} \sum \frac{(O_i - M_i)^2}{\sigma^2} \quad (3)$$

where N_{pix} is the number of pixels used and σ is determined by the S/N of the spectrum. Table 1 details the diagnostic lines used in this analysis. The wavelength range over which to compute the χ^2 is important to consider. If the range is too small, the wings of the lines will be neglected, which would lose vital information which is used to contstrain the model parameters. For example, microturbulance most affects the wings of the diagnostic lines. **Confirm this!** However, if too much of the psuedo-continuum is included, the parameters could be biased by noise features in the observations. The regions which are taken for the χ^2 calculation is shown in figure 4. There are multiple cases where the diagnostic lines are sufficiently close together that, at $R \sim 3000$

Each observed spectrum is cross-correlated before the χ^2 calculation is performed with a rest wavelngth spectrum. Additionally, each observed-model spectra pair is cross-correlated prior to the calculation, an estiamte of the offset between the two spectra is calcaulted using an iterative approach and the offset is applied to the observed spectrum to ensure the central wavelengths of the lines are at rest wavelenght. The cross-correlation shift between each observed-model spectra pair is typically $\sim 0.01\text{pix}$.

Each parameter is selected based on a weighted average, where the weights are determined by the χ^2 value of the model:

$$w = \exp(-\chi^2/2) \quad (4)$$

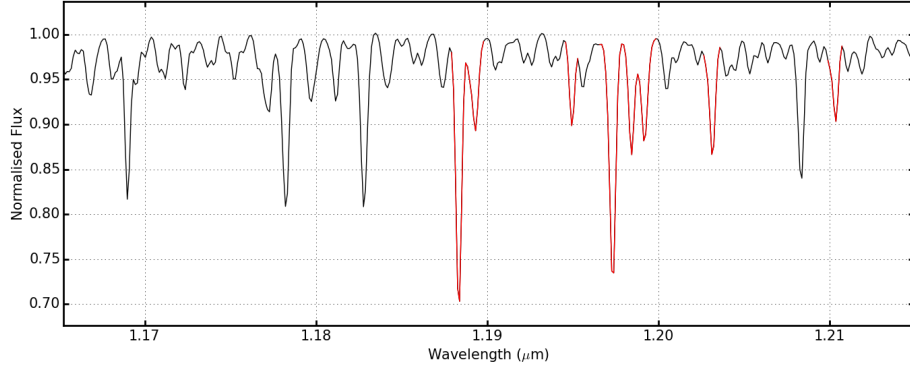


Figure 4 *An example of a model spectrum, degraded and resampled to that of a typical observed spectrum (in this case NGC6822-RSG01), where the regions used to compute the χ^2 calculation is highlighted in red.*

Table 1 *Diagnostic lines*

Species	Line Centre
Fe I	1.188285
Fe I	1.197305
Si I	1.198419
Si I	1.199157
Si I	1.203151
Si I	1.210353
Ti I	1.189289
Ti I	1.194954
Mg I	
Mg I	

The average is performed over 100 models with the lowest χ^2 value. **Need to define some parameter stability tests and show that 100 is a good amount of models to use.**

Errors on the parameters are determined by defining $\Delta\chi^2 = \chi^2_{min} + 3$. The standard deviation of the models parameters for all models which have a χ^2 value within this range define the errors.

The significance of the 3 is that given that there are 8 diagnostic lines,

0.4 Testing

0.5 Conclusions

References

Bergemann, M., Kudritzki, R.-P., Gazak, Z., Davies, B., and Plez, B. (2014).

- Red Supergiant Stars as Cosmic Abundance Probes. III. NLTE effects in J-band Magnesium lines. *ArXiv e-prints*.
- Bergemann, M., Kudritzki, R.-P., Plez, B., Davies, B., Lind, K., and Gazak, Z. (2012). Red Supergiant Stars as Cosmic Abundance Probes: NLTE Effects in J-band Iron and Titanium Lines. , 751:156.
- Bergemann, M., Kudritzki, R.-P., Würl, M., Plez, B., Davies, B., and Gazak, Z. (2013). Red Supergiant Stars as Cosmic Abundance Probes. II. NLTE Effects in J-band Silicon Lines. , 764:115.
- Cunha, K., Sellgren, K., Smith, V. V., Ramirez, S. V., Blum, R. D., and Terndrup, D. M. (2007). Chemical Abundances of Luminous Cool Stars in the Galactic Center from High-Resolution Infrared Spectroscopy. *ApJ*, 669:1011–1023.
- Davies, B., Kudritzki, R.-P., and Figer, D. F. (2010). The potential of red supergiants as extragalactic abundance probes at low spectral resolution. *MNRAS*, 407:1203–1211.
- Davies, B., Origlia, L., Kudritzki, R.-P., Figer, D. F., Rich, R. M., and Najarro, F. (2009a). The Chemical Abundances in the Galactic Center from the Atmospheres of Red Supergiants. *ApJ*, 694:46–55.
- Davies, B., Origlia, L., Kudritzki, R.-P., Figer, D. F., Rich, R. M., Najarro, F., Negueruela, I., and Clark, J. S. (2009b). Chemical Abundance Patterns in the Inner Galaxy: The Scutum Red Supergiant Clusters. *ApJ*, 696:2014–2025.
- Evans, C. J., Davies, B., Kudritzki, R.-P., Puech, M., Yang, Y., Cuby, J.-G., Figer, D. F., Lehnert, M. D., Morris, S. L., and Rousset, G. (2011). Stellar metallicities beyond the Local Group: the potential of J-band spectroscopy with extremely large telescopes. *A&A*, 527:A50.
- Gazak, J. Z., Davies, B., Kudritzki, R., Bergemann, M., and Plez, B. (2014). Quantitative Spectroscopic J-band study of Red Supergiants in Perseus OB-1. , 788:58.
- Gustafsson, B., Edvardsson, B., Eriksson, K., Jørgensen, U. G., Nordlund, Å., and Plez, B. (2008). A grid of MARCS model atmospheres for late-type stars. I. Methods and general properties. *A&A*, 486:951–970.